



3D printed, plastic photocatalytic flow reactors for water purification

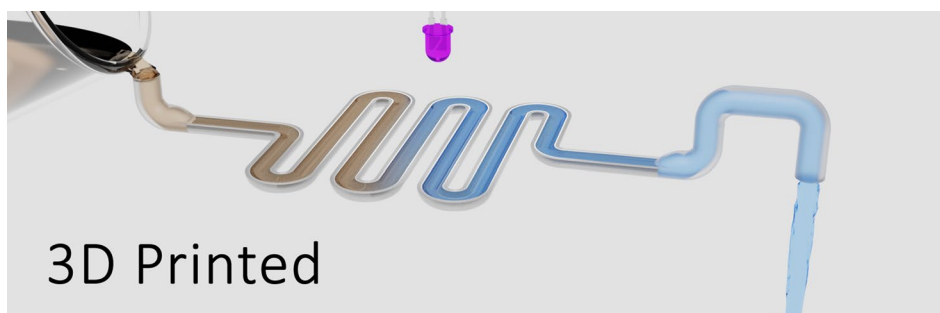
Ruicheng Zhou¹ · Ri Han¹ · Michael Bingham¹ · Christopher O'Rourke¹ · Andrew Mills¹

Received: 4 February 2022 / Accepted: 3 May 2022 / Published online: 24 May 2022
© The Author(s) 2022

Abstract

3D printing is known as a fast, inexpensive, reproducible method for producing prototypes but is also fast becoming recognised as a scalable, advanced manufacture process. Two types of lab-scale, 3D printed plastic, fixed-film, flow-through photocatalytic reactors are described, both of which are sinusoidal in shape, and only differ in that one has no baffles, reactor **A**, whereas the other has, reactor **B**. Both reactors are lined with a P25 TiO₂/polylactic acid (PLA) coating, which, after UVA pre-conditioning, is used to photocatalyse the bleaching of circulating aqueous solutions of either methylene blue, MB, or phenol, PhOH, repeatably, without any obvious loss of activity. The rate of the photocatalysed bleaching of MB exhibited by reactor **B** shows a much lower dependence upon flow rate than reactor **A**, due to the greater lateral mixing of the laminar flow streams produced by the baffles. The photonic efficiencies of reactor **A** for the photocatalysed bleaching of MB and PhOH were determined to be 0.025% and 0.052%, respectively, and the photocatalytic space-time yields (PSTY) to be 0.98×10^{-4} and 1.49×10^{-4} m³ of reaction solution.m⁻³ reactor volume.day⁻¹.kW⁻¹, respectively. This is the first example of an all plastic, 3D printed photocatalytic reactor and demonstrates the advantages of 3D printing for prototyping. Given the 3D printing is a scalable process, possible potential areas of application are discussed briefly.

Graphical abstract



Keywords Photocatalysis · 3D printed reactors · Baffles · Titanium dioxide · Fixed-film · UV · Organic pollutants

1 Introduction

Photocatalysis as a method for treating and purifying water continues to be of interest [1]. Its attractive features include its ability to oxidatively mineralise most organic pollutants and utilise sunlight. Invariably, the photocatalyst employed

is TiO₂, due to its high activity, low cost and chemical and biological inertness. Indeed, the only major drawback to using TiO₂ is its large band gap (3.2 eV for anatase TiO₂), which means it can only utilise solar UV, which represents *ca.* 4% of the energy in the solar spectrum [2].

Photocatalytic reactors can be broadly sub-divided into two types, those that use the photocatalyst in suspended form, *i.e.* slurry reactors, and those that use it in immobilised form, *i.e.* fixed-film reactors [3, 4]. Slurry reactors require a photocatalyst recovery and reuse stage which is technically challenging and adds to the overall cost of water

✉ Andrew Mills
andrew.mills@qub.ac.uk

¹ School of Chemistry and Chemical Engineering, Queens University Belfast, Stranmillis Road, Belfast BT9 5AG, UK

treatment. Clearly photocatalyst recovery is not a problem with fixed-film reactors, but these in turn can exhibit low efficiencies due to low photocatalyst surface area and mass transfer issues. Proposed routes to solve these issues include the use of foam photocatalysts or microreactors [5].

Another potential limitation of fixed-film, photocatalytic reactors is the choice of supporting substrate in that it has to be able to sustain the elevated temperatures often used to immobilise or coat the photocatalyst. Although an early approach to photocatalyst coating was to dry a wet-coating of an aqueous dispersion of the photocatalytic powder with warm air [6], such coatings are not robust [3, 7]. As a result, most coating methods, including those that use photocatalyst powders, involve a final high temperature annealing step, typically 450 °C for 1 h [8, 9]. Other popular coating methods include sol-gel [7] or colloid deposition [10], anodisation [11] and electrophoretic deposition [9]. Invariably, the support substrate is glass or a metal, such as stainless steel, i.e. a material that can withstand the final high temperature annealing step used to improve coating adherence [9]. However, such materials restrict the design of most photocatalyst reactors to that of simple plates or tubes, to which it is difficult to add features, such as baffles, which will improve lateral flow mixing and so reduce any dependence of the kinetics on mass transport.

Interestingly, there appears to be no reports of an all-plastic photocatalytic flow reactor, even though there are many reports of photocatalyst-coated plastic films, deposited using a variety of techniques including, sol-gel dip-coating [12], powder plasma spray [13], powder dip-coating [14], magnetron sputtering [15], and atomic layer deposition [16]. However, most of these coating methods are not conducive, either practically or in terms of cost, to the creation of the internal photocatalytic coating required for a fixed-film flow-through photocatalytic reactor.

In recent years, there have been a few reports concerning the production of photocatalytic plastic films by extrusion [17–19], which is also a fundamental step in the production of the polymer filament used in 3D printing. 3D printing embraces many different technologies, the most popular of which is fused deposition modelling, FDM. In FDM, a temperature-controlled head extrudes the polymer, layer by layer, onto the printing platform. The path of the printing head is computer-controlled, allowing a myriad of subtly different designs of large and small objects alike to be printed quickly, reproducibly and usually at little cost. Common materials used in this type of 3D printing include, acrylonitrile butadiene styrene (ABS), polycarbonate (PC) and polylactic acid (PLA). Although used initially to fabricate models and prototypes, 3D printing is fast becoming a method for mass manufacture. The advantages 3D printing have over most other methods of manufacture include, speed of production of final item, low initial capital investment

cost, greater flexibility in product design and changing product design, low material waste and often a low production cost per item, since it usually involves single step manufacture and near zero labour costs [20]. There have been a few reports of 3D printed photocatalytic objects, mainly as filters and meshes [19, 21–25] but, none of a 3D printed photocatalytic reactor. This work describes the production, UV activation and subsequent initial testing of two different 3D printed photocatalytic reactors, one with baffles, and one without, where the performance of each is probed using two different test organic pollutants, namely, methylene blue, MB and phenol, PhOH, which are commonly employed to test photocatalytic reactors, as indicated by the long list of examples given in Table S1 in the electronic supplementary information (ESI) file [26–51]. To our knowledge, this is the first example of plastic-based, 3D printed photocatalytic reactor.

2 Experimental

2.1 Materials

The key materials used in this study were polylactic acid, PLA, pellets (3DQF, Leigh, UK), P25 TiO₂ nanoparticles (Evonik Industries, Essen, Germany), methylene blue, MB, (Merk Life Science UK Ltd., Gillingham, UK), phenol (Merk Life Science UK Ltd., Gillingham, UK) and HCl (Fisher Scientific, Hampton, USA). All aqueous solutions were made up using doubly distilled, de-ionised water.

2.2 Methods

2.2.1 3D printed filament production

The two different filaments used in this work, namely, one comprising just PLA and the other comprising PLA with 5 wt.% TiO₂, were produced using a 3devo filament maker - composer 350 (3devo B.V., Utrecht, Netherland). The method used to produce the filaments was based on the conditions reported elsewhere for PLA filament production [52, 53] and the 3devo's on-line guide to filament production [54]. The PLA-only filament was made by adding the PLA masterbatch pellets to the filament maker, which had a pre-heated mixing chamber set at 190 °C and extruding them as a filament, using an extruder screw speed of 3.5 rpm to ensure the diameter of the filament was the required value of 1.75 mm.

To make the 5 wt.% TiO₂/PLA filament, first a masterbatch of 5 wt.% TiO₂/PLA pellets had to be generated using a different extruder, Rondol Microlab 10 mm twin screw extruder, designed for pellet and film manufacture. Thus, the 5 wt.% TiO₂/PLA masterbatch pellets were made by first

mixing 1 g of the P25 TiO₂ nanoparticulate powder with 19 g of the PLA pellets and then blending the mix together, using the Rondol Microlab extruder, to produce a filament, ca. 2 mm in diameter, which was subsequently cut up into 3 mm long pellets. The temperature applied on the Rondol Microlab extruder was 170 °C and the extruder was operated at a screw speed of 70 rpm. These pellets were put through the extruder two more times to ensure that the TiO₂ was dispersed uniformly throughout the PLA in the 5 wt.% TiO₂/PLA masterbatch of pellets. These pellets were then used to produce the 1.75 mm diameter, 5 wt.% TiO₂/PLA filament for 3D printing using a 3devo filament maker—composer 350 (3devo B.V., Utrecht, Netherland), operated under the same conditions as described above for the PLA-only filament.

2.2.2 3D photocatalytic reactor production

Two different 3D printed, plastic, sinusoidal, flow-through photocatalytic reactors were produced and used in this work, namely one *without* and one with *baffles*, i.e. reactors **A** and **B**, respectively. Both were produced using a Raise3D Pro2 dual-extruder 3D printer (Raise3D, Irvine, California, US), with the appropriate 1.75 mm diameter filament. The printing speed was 20 mm s⁻¹ and the temperature of the printing platform was 60 °C. The dual nozzle temperature was either 175 °C, or 170 °C, when using the PLA or 5 wt.% TiO₂/PLA filament, respectively. The total printing time was 135, or 150 min, for the *without*, or *with*, *baffles* reactors, respectively. The two different sets of G-code used by the 3D printer to print the two different reactors can be downloaded at the following website [55].

A schematic illustration of the basic photocatalyst reactor, i.e. one with no baffles, reactor **A**, used in most of this work is given in Fig. 1. A similar schematic illustration of the two reactors, and the associated very different reaction solution flow patterns, is given in Figure S1 in the ESI file. In both cases, the reactor comprised a sinusoidal-shaped, semi-circular, PLA gutter, lined with a 0.5 mm thick 5 wt.% TiO₂/PLA film. The thickness of the PLA gutter wall was 1 mm. In the 3D printing process, the lined PLA gutter was set and sealed onto a 100 µm thick, flat PLA film so as to create a flat-covered semi-circular gutter-shaped channel through which the reaction solution under test could be pumped, see Figs. 1 and S1 in the ESI. All UV irradiations were through the 100 µm PLA film, which is henceforth referred to as the ‘PLA window’. The radius and length of the TiO₂-lined part of the gutter channel were 1.5 mm and 37.2 cm, respectively; the volume of reaction solution in the TiO₂-lined part of the reactor was 1.31 cm³. As indicated by the schematic illustrated in Fig. S1, in the ESI, reactor **B**, was otherwise identical to reactor **A**, but with an additional 35 equally spaced, 1 cm apart, PLA baffles, each of which

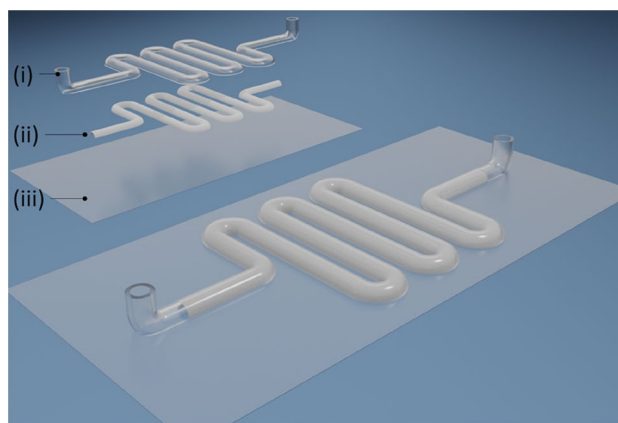


Fig. 1 Schematic illustration of reactor **A**, which comprised (i) a 1 mm thick PLA gutter, mostly lined with (ii) a 0.5 mm thick coating of 5 wt.% TiO₂/PLA, sealed onto (iii) a 100 µm PLA film; the ‘PLA window’

covered half the cross-sectional area of the gutter, i.e. a quarter circle of radius 1.5 mm, and was 600 µm thick. These baffles were used to disrupt the flow of the reaction solution and so improve lateral mixing. Table S2 in the ESI provides a summary of the various design features of the two reactors.

A Masterflex L/S peristaltic pump, purchased from the Cole-Parmer Instrument Company (St. Neots, UK) was used to pump the reaction solution through the photocatalytic reactor under test and on to a quartz flow-through cuvette (Hellma Analytics, Southend-on-Sea, UK) with a 1 cm path length. The latter allowed the concentration of MB, or phenol, i.e. [MB] or [PhOH], in the reaction solution exiting the photoreactor to be monitored spectrophotometrically as a function of irradiation time.

2.2.3 Other methods

2.2.3.1 UV pre-conditioning The UV pre-conditioning of each of the photocatalytic reactors was carried out using two, 352 nm UVA light (15 W BLB bulbs) with an incident irradiance of ca. 1.5 mW cm⁻². In this work, the UVA fluorescent tubes were used so as to provide a long-lived, a stable, uniform irradiance for up to 168 h.

2.2.3.2 UV irradiation in kinetic runs In all the photocatalytic kinetic runs reported here, a 2.8 W, 365 nm UVA LED (RS, Corby, UK), was used as the UV source, rather than the BLBs used in the pre-irradiation step, because they were able to provide the high irradiances needed to generate photocatalytic rates which could be measured *via* UV/Vis spectrophotometry. Thus, in the photocatalyzed bleaching of MB, and the destruction of phenol, the power supplied to the UVA LED was usually adjusted so as to provide an incident irradiance of 15, and 40, mW cm², respectively, where

all UV irradiances were measured using a Hamamatsu UV power meter.

2.2.3.3 UV/Vis spectroscopy All UV/Vis absorption spectra, including these of the reaction solution, were recorded using Cary 50 UV/Vis spectrophotometer (Varian, Santa Clara, USA).

2.2.3.4 Scanning electron microscopy All SEM images were acquired using a recorded field-emission gun scanning electron microscope, i.e. FEG-SEM, (JEOL JSM-6500F).

2.2.3.5 Contact angle measurements Water droplet contact angle measurements were made using a FTA32 instrument (First Ten Angstrom, Newark, USA). In this work, each of the sample films tested was stuck to a microscope slide using double sided tape, a 13 μL water droplet was then deposited onto the sample's surface and allowed to equilibrate for 1 min before the contact angle was then measured. Each sample was tested in this way five times and the average value reported.

3 Results and discussion

3.1 UV pre-conditioning

In an earlier paper on extruded thin films of low-density polyethylene, LDPE, loaded with P25 TiO_2 , it was found that the extruded films exhibited little or no photocatalytic activity because the embedded TiO_2 particles were covered with the polymer [18]. As a consequence, these films required 'activation' with UV radiation before they could be used to effect the desired photocatalytic reaction. Such UV pre-conditioning allows the TiO_2 particles at, or near, the surface to photocatalytically oxidise the thin layer of polymer covering them, so as to reveal a photocatalytically active surface [18]. The need for UV pre-conditioning is common in many commercial photocatalytic products, including photocatalytic paints from STO [56, 57] and curtains from IKEA [58, 59]. This step and subsequent use of the activated film to drive the photocatalytic reaction of interest, such as the removal of NO_x or VOCs, has the beneficial effect of continually refreshing the photocatalytic surface, although the logical downside of this feature is that ultimately it must lead to the complete loss of the photocatalytic layer. However, provided the embedding polymer is very resistant to photocatalytic oxidation, and therefore slow to be mineralised photocatalytically, this loss process is likely to take a long time; indeed, apparently years for commercial photocatalytic paints and curtains [57, 59].

It follows from above that the 3D printed TiO_2/PLA lining of the 3D printed photocatalytic reactor, see Fig. 1, will

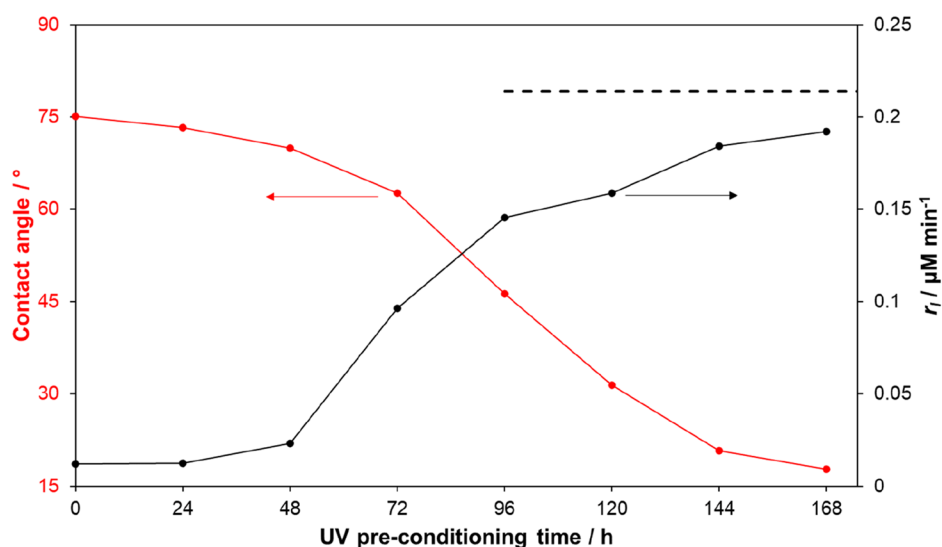
require UV pre-conditioning if it is to be tested under optimum conditions of activation. It is, of course, possible to identify the UV pre-conditioning time, t_{con} , that would provide a surface of optimum activity using the reactor itself. But this was judged to be too time-consuming, since for each value of t_{con} tried, a new reactor would need to be, (i) printed, which takes ca. 135 min and consumes a lot of filament and (ii) tested, which typically takes 210 min. Thus, to identify *quickly* the length of time required to achieve a high level of activation of the TiO_2/PLA layer, i.e. an approximate value for t_{con} , a number of identical, rectangular 5 wt.% TiO_2/PLA films (12.5 mm \times 8 mm; 100 μm thick) were printed using an Ultimaker 3 3D printer (Ultimaker B.V., Utrecht, Netherlands) and then UV-pre-conditioned for different times, up to 168 hours, before being tested for photocatalytic activity. An added advantage of this approach to determine the value of t_{con} is that the physical changes on the surface of the TiO_2/PLA layer that UV pre-conditioning brings about can be probed readily through contact angle measurements and using SEM.

Note that, since the UV pre-conditioning step of the TiO_2/PLA film in the reactor must occur *in situ*, it follows that all the rectangular test samples needed to be UV irradiated though a 100 μm PLA sheet film, to simulate the PLA window of reactors **A** and **B**. Although the 3D printed, 100 μm thick PLA sheet film absorbs little UVA irradiation, it is quite scattering and has an absorbance at 365 of 0.23, as revealed by the plot of its UV/Vis absorption spectrum illustrated in Fig. S2 in the ESI. Also illustrated in Fig. S2 are the emission spectrum of the UVA LED used in all the photocatalytic runs and the diffuse reflectance spectrum of the P25 TiO_2 photocatalyst used to make the TiO_2/PLA film, which overlaps significantly with the LED's emission spectrum.

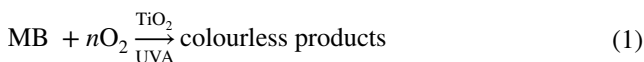
The photocatalytic activities of the 3D printed, rectangular TiO_2/PLA films, UV pre-conditioned for different times, were assessed by monitoring for each film its ability to bleach photocatalytically a MB aqueous solution. In this work, the rectangular TiO_2/PLA film under test was placed in a 1 cm stirred cuvette, which contained 3.5 cm^3 of the MB solution, 10 μM . This system was then irradiated with UVA (365 nm, 15 mW cm^{-2}) radiation and the photocatalysed bleaching of the MB was monitored spectrophotometrically. Further details of this MB test system are given in S3 in the ESI, which is effectively a modified version of the MB-based ISO for assessing photocatalytic films [60–63]. From this work, the initial rate of the photocatalysed bleaching of MB, r_i , was determined for each of the TiO_2/PLA films, pre-irradiated with UV radiation for different times, t , and a plot of the results in the form of r_i vs. t is illustrated in Fig. 2.

Although the photocatalysed oxidative mineralisation of MB, to HCl, HNO_3 , H_2SO_4 , CO_2 and water, by TiO_2 is well established [64], the generation of CO_2 occurs on a longer timescale than the photocatalysed bleaching of MB. This

Fig. 2 Plot of the measured water droplet contact angle (red line) and the initial rate of bleaching of MB (black line), r_i , as a function of UV pre-conditioning time for the 5 wt.% TiO₂/PLA films in a 1 cm cuvette. The broken line represents the measured initial rate for a highly active sol-gel TiO₂ film on glass, identical in size and shape to that of the TiO₂/PLA films



observation suggests that the MB is initially photocatalytically oxidised to colourless products, which are then oxidised further, eventually to the minerals. Houas et al. have carried out a detailed study of the photocatalysed mineralisation of MB and found evidence that the first step is the oxidation of the C-S⁺=C group in MB by a photogenerated hydroxyl radical to form a sufoxide and that this process opens up the central aromatic ring, with the concomitant loss of colour [65]. As a result, the photocatalysed bleaching of MB studied in this work, and most other studies using MB as a test pollutant, including the MB ISO [60], can be best summarised as follows,



The results illustrated in Fig. 2 show that the 5 wt.% TiO₂/PLA film is activated markedly with increasing UV pre-conditioning time and that after 168 h UV pre-conditioning the photocatalytic activity of the film is near to a maximum value. Figure 2 also shows the measured value of r_i ($=0.21 \mu\text{M min}^{-1}$) for a highly active TiO₂ sol-gel film [66] on glass slide of the same size and shape as the TiO₂/PLA rectangular films, i.e. 12.5 mm × 8 mm. It would appear from the results for the UV pre-conditioning TiO₂/PLA films illustrated in Fig. 2, that with further UV pre-conditioning, the activity of the film would approach a value of r_i similar to that exhibited by the TiO₂ sol-gel film.

In this system, it is likely that the apparent maximal rate of $0.21 \mu\text{M min}^{-1}$ exhibited by the rectangular 12.5 mm × 8 mm TiO₂ sol-gel film is due to mass transport control, and so is a measure of the rate of diffusion of the MB from the bulk of the reaction solution to the surface of the photocatalyst. Further evidence that the high similar rates exhibited by TiO₂ sol-gel film and the 5 wt.% TiO₂/PLA film UV pre-conditioned for 168 h, are largely limited by mass transport

is the observation that they both increase with increasing stirrer speed, as expected for a diffusion-controlled, but not activation-controlled, reaction, since in the former case, the diffusion-layer thickness, b , will decrease with increasing solution agitation/flow rate, *vide supra* [46]. The measured variation of r_i for the 5 wt.% TiO₂/PLA film UV pre-conditioned for 168 h, as a function of stirrer speed is illustrated in Fig. S5 in the ESI.

The observation that the rate of reaction (1), as measured for a photocatalytic film in a stirred reaction solution, appears to reach a value that is limited by the rate of diffusion of the MB to the surface of the photocatalytic film is not surprising, since mass transport is recognized as a problem in the assessment of the activity of photocatalytic films using the MB ISO [60, 63]; the set up for which is very similar to that used here, as noted earlier. Indeed, others have studied this problem in some detail [63], and estimated that the initial diffusion-controlled rate in such a system, r_D , is given by the following expression,

$$r_D (\text{units M min}^{-1}) = 0.06 \cdot D_{MB} \cdot [\text{MB}] \cdot A / (b \cdot V) \quad (2)$$

where, D_{MB} is the diffusion coefficient for MB ($6.74 \times 10^{-6} \text{ cm}^2 \text{ s}^{-1}$) [67], $[\text{MB}]$ is the initial bulk concentration of MB ($10 \mu\text{M}$ in this work), A is the photocatalyst surface area (1 cm^2), b is the diffusion layer thickness (estimated as 0.01 cm [63, 68]) and V is the reaction solution volume ($3.5 \times 10^{-3} \text{ dm}^3$). Using this equation, and the above values for the various parameters used in this work, a value for r_D of $0.12 \mu\text{M min}^{-1}$ can be generated for our MB test system conducted using a 1 cm cuvette as the reactor, which is not too dissimilar to the maximum measured value found, i.e. $0.21 \mu\text{M min}^{-1}$, *vide supra*. The discrepancy in the measured and calculated values of initial rate is probably due to the value chosen for the diffusion layer thickness, δ , namely $100 \mu\text{m}$,

in the calculation of r_D . This value is an appropriate, approximate value of b for a non-stirred solution [68], as is the case in the MB ISO [60], however, in this work, the reaction solution was stirred and so b should be much smaller. Indeed, if a value of $55 \mu\text{m}$ is used instead as the value of b in Eq. (2), then the calculated value for r_D is the same as the value of $0.21 \mu\text{M min}^{-1}$ measured in this work. The observation that r_i for the 5 wt.% TiO_2/PLA film UV pre-conditioned for 168 h increases with stirrer speed, see Figure S5 in the ESI, is consistent with Eq. (2), since b decreases with increasing solution agitation/flow rate [68].

Indirect evidence of the significant disruption of the surface of the TiO_2/PLA film, with concomitant exposure of the underlying TiO_2 photocatalyst particles, produced by the UV pre-conditioning step, is provided by the measured change in water droplet contact angle, CA, exhibited by the films as a function of UV pre-conditioning time, the results of which are illustrated in Fig. 2. PLA is quite a hydrophobic material, with a water droplet contact angle of ca. 80° [69] whereas P25 TiO_2 , is highly hydroxylated, and super-hydrophilic, i.e. with a CA value of $<10^\circ$ [70]. Thus, it is no surprise that with increasing UV-pre-conditioning the measured value of CA exhibited by the TiO_2/PLA film drops significantly from an initial value of 75° to ca. 18° after 168 h exposure to 1.5 mW cm^{-2} UVA radiation. The results illustrated in Fig. 2 suggests that the variation in CA with UV pre-conditioning time is negatively correlated with r_i , i.e. photocatalytic activity. Such a correlation has been noted previously [18, 70] for TiO_2 films and suggests that in such systems, the value of the reciprocal of CA provides a rough measure of the level of surface exposed TiO_2 particles [18].

Direct evidence of the significant surface disruption and TiO_2 photocatalyst particle exposure brought about by UV

pre-conditioning is provided by scanning electron microscopy, SEM. An illustrative sample of the micrographs recorded for TiO_2/PLA films, UV pre-conditioned for different times, is illustrated in Fig. 3.

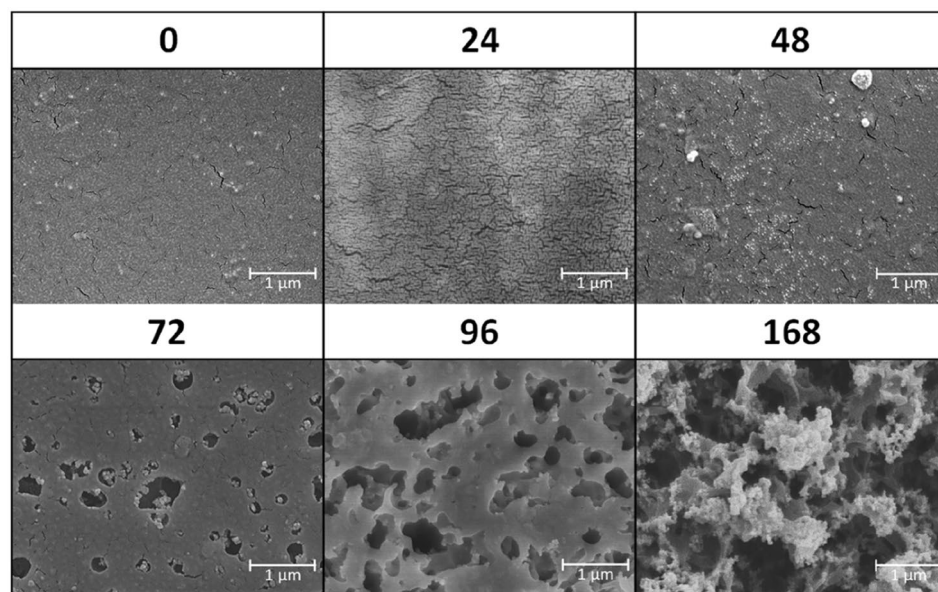
The images in Fig. 3 reveal why there is little change in CA even with 48 h UV pre-conditioning time (see Fig. 2), since up to that point, the surface is largely unchanged and so retains much of the hydrophobic nature of PLA. It is also clear from the SEM images in Fig. 3 why in Fig. 2 the CA drops markedly after 48 h UV pre-conditioning, because it is associated with an increasing degree of pitting of the surface, and exposure of the underlying TiO_2 particles, with increasing UV pre-conditioning. The above results show that 168 h UVA pre-conditioning of a TiO_2/PLA film significantly disrupts the surface, leaving many photocatalytic TiO_2 particles exposed and able to bleach MB photocatalytically at near to a mass-transport controlled rate. As a consequence, both the photocatalytic reactors A and B were always pre-conditioned with 168 h UVA before use.

3.2 Photocatalytic reactor A: single pass studies

Photocatalytic reactor A was connected to a peristaltic pump that drew from a reservoir an air-saturated MB aqueous solution ($10 \mu\text{M}$ in 0.01 M HCl) and flowed it through the reactor and into a 1 cm pathlength, flow-through UV/Vis spectrophotometer cell and then into a waste solution beaker. A schematic illustration of the system is given in Fig. 4.

This single pass system allowed the change in the absorbance at 665 nm of the reaction solution, Abs_{665} , due to the photocatalysed bleaching of MB, i.e. ΔAbs_{665} , to be measured at different reaction solution flow rates, f . The plot of the observed change in Abs_{665} with lights off (black lines)

Fig. 3 Scanning electron micrographs of the TiO_2/PLA film UVA pre-conditioned (1.5 mW cm^{-2}) for different times (given in hours above each image)



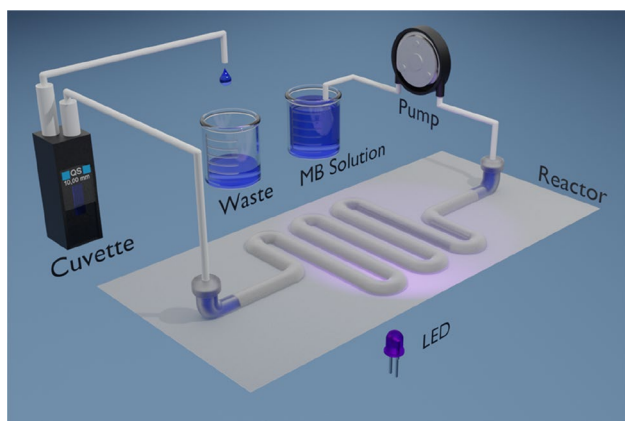


Fig. 4 Schematic illustration of the single pass flow through system used to test reactors **A** and **B**. Note that UV irradiation of the 3D printed reactor (365 nm LED, 15 mW cm^{-2}) is from below, through the $100\text{ }\mu\text{m}$ PLA sheet to which the photocatalyst lined, semi-circular ‘gutter’ was sealed

and lights on (red lines) at different f values, from 1 to $80\text{ cm}^3\text{ min}^{-1}$ are illustrated in Fig. 5a. These results allowed the subsequent generation of the plot of ΔAbs_{665} vs f illustrated in Fig. 5b.

The average rate of the photocatalysed bleaching of MB, r , that occurs in the reactor can be calculated using the following expression,

$$r = \Delta\text{Abs}_{665} \cdot f / (\epsilon(\text{MB}) \cdot V_r) \quad (3)$$

where $\epsilon(\text{MB})$ is the molar absorptivity of MB at 665 nm (determined to be $82400\text{ M}^{-1}\text{ cm}^{-1}$) and V_r is the volume of the reaction solution exposed to the TiO_2/PLA photocatalytic lining (1.31 cm^3). In Eq. (3), the ratio, $\{\Delta\text{Abs}_{665}/\epsilon(\text{MB})\}$ is

the steady-state change in concentration of MB in the reaction solution, $[\text{MB}]$, upon irradiation of the reactor, operating at a flow rate, f . Using the data in the main diagram in Fig. 5b, the plot of r vs f was constructed and is illustrated in the insert diagram in Fig. 5b. At low flow rates, it is likely that the average rate of reaction, r , for reaction (1) will be controlled to some extent by the rate of mass transport, r_{mt} , of the MB in the bulk of the flowing reaction solution to the photocatalytic film, as well as that due to the rate of photocatalysis at the surface of the TiO_2/PLA film, r_{pc} . Under such circumstances, the overall measured rate, r , is related to these two parameters via the following expression [71],

$$1/r = 1/r_{mt} + 1/r_{pc} \quad (4)$$

The rate of mass transport is flow rate dependent, and typically, for a cylindrical reactor, is proportional $f^{1/3}$ [72]. Thus, strong evidence that a component of the measured overall rate for a photocatalytic reactor is due to mass transport control is usually derived from its r vs f profile, which would be expected to show a continual increase in r with increasing f [6, 64, 71]. In contrast, a brief inspection of Eq. (4) reveals that if r appeared independent of f above some threshold value, this would indicate $r_{mt} \gg r_{pc}$, and that the rate determining step is effectively the rate of photocatalysis, i.e. $r = r_{pc}$. A brief inspection of the r vs f plot in Fig. 5b suggests that the threshold value of f for photoreactor **A** is ca. $40\text{ cm}^3\text{ min}^{-1}$ and at this and higher flow rates the measured rate of photocatalysis is activation controlled for reaction (1) in this system. As a consequence, $f = 40\text{ cm}^3\text{ min}^{-1}$ was used in all subsequent work involving this reactor.

As noted above, see also Fig. 5b, in this work, the flow rate was varied from 1 to $80\text{ cm}^3\text{ min}^{-1}$, representing

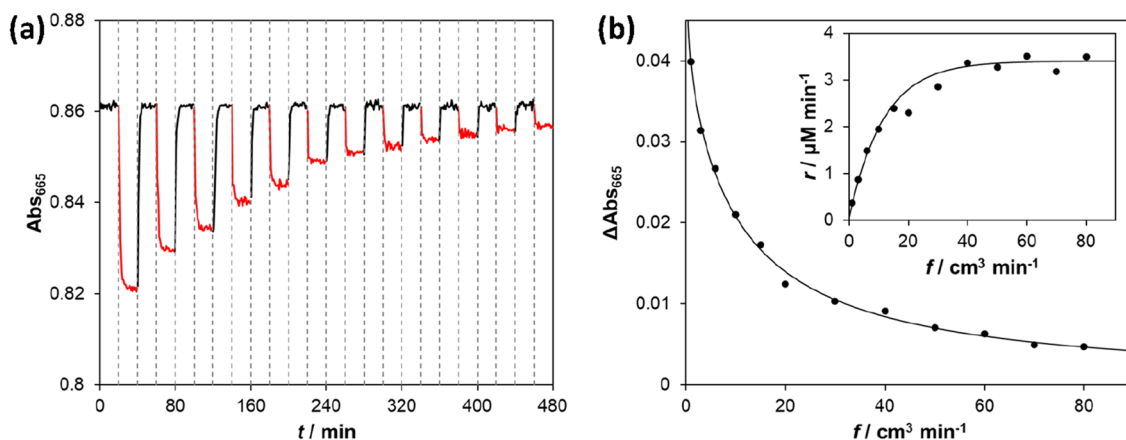


Fig. 5 a Measured variation in the absorbance at 665 nm due to the MB reaction solution flowing out of reactor **A** under light off (black lines) and light on (red lines) conditions at the following values of f ; (from left to right): $1.3, 6, 10, 15, 20, 30, 40, 50, 60, 70$ and 80 cm^3

min^{-1} , **b** plot of the data in (a) in the form of ΔAbs_{665} vs flow rate, f . The insert plot is that of the average rate of reaction (1), r , calculated using the ΔAbs_{665} data in the main diagram and Eq. (3), vs f . In all this work, the incident UVA irradiance was 15 mW cm^{-2}

Reynolds number, Re , values from 8 to 636, given that, for a straight tube,

$$Re = f\rho/(15.\pi\mu d) \quad (5)$$

where f is the flow rate ($\text{cm}^3 \text{min}^{-1}$), ρ = density of water (g cm^{-3}), μ = kinetic viscosity of water ($8.9 \times 10^{-3} \text{g cm}^{-1} \text{s}^{-1}$) [73] and d is the diameter of the tube (0.4 cm). These low values of Re indicate that the photocatalytic reaction was carried out in a laminar, and not turbulent, flow regime at all flow rates used in this work, since turbulent flow is usually considered to transition at a Re value of ca. 2100 for such tubes [71].

The quantum efficiency, δ , of reactor **A** for the photobleaching of MB, when used in single pass mode, is readily calculated, given,

$$\delta = r.V_r.N_A/\text{Incident UVA intensity}, I_{UV} \quad (6)$$

where r is the average rate (here, ca. $3.4 \mu\text{M min}^{-1}$, see Fig. 5b), V_r is the volume of reaction solution in contact with the TiO_2/PLA lining (1.31cm^3), N_A = Avogadro's number, and $I_{UV} = 6 \times 10^{10}.\alpha.\rho_{UV}.A_r$ (units: photons min^{-1}), with $\alpha = 1.84 \times 10^{15}$, i.e. the factor for converting mW cm^{-2} to number of photons of 365 nm radiation per cm^2 , ρ_{UV} = incident UV photon flux/UV irradiance (15mW cm^{-2}) and A_r = cross-section area of TiO_2 coated lining (11.2cm^2). Using the above values reveals a photonic efficiency of ca. 0.015% for reactor **A**, which compares favourably with the value of 0.047% reported by Tschirch et al. for P25 TiO_2 coated glass when tested using the MB ISO, using $[\text{MB}]_0 = 10 \mu\text{M}$ and $\rho_{UV} = 1 \text{mW cm}^{-2}$ [60, 74]. However, it is worth noting again at this point that the $100 \mu\text{m}$ PLA window, through which the incident UV irradiance must pass, is slightly opaque, due to light scattering, and has an absorbance of ca. 0.23 at 365 nm, which suggests the UV irradiance incident on the TiO_2/PLA film is actually ca. 9.0 (rather than 15) mW cm^{-2} and so the actual photonic efficiency of reactor **A** is probably nearer ca. 0.025%.

The kinetics of the photocatalysed oxidation of most organic pollutants by ambient O_2 fit an equation with the following general form,

$$r = kK[\text{P}]/(1 + K[\text{P}]) \quad (7)$$

where r is the measured rate of photocatalysis, k is the maximum rate and K is an *apparent* constant, when the incident UV irradiance and concentration of oxygen are fixed, and $[\text{P}]$ is the concentration of organic pollutant. When $[\text{P}]$ and $[\text{O}_2]$ are fixed, r , and so k , is usually found to be related to the irradiance via the following expression,

$$k = \beta\rho_{UV}^\theta \quad (8)$$

where β is a proportionality constant and θ is a constant, the value of which depends upon ρ_{UV} , and often equal to 0.5 and 1 at high and low values ρ_{UV} , respectively [2]. Equations (7) and (8), often referred to as the *apparent* Langmuir-Hinshelwood (LH) equation, is an *empirical* equation that describes a system that exhibits saturation kinetics; thus, the 'constants' in Eqs. (7) and (8), are parameters that provide the best fit to the kinetic data, and provide little insight into the underlying mechanism. Consequently, Eqs. (7) and (8) are used here to fit the data and so aid comparison between the kinetics exhibited by two closely related 3D printed photocatalytic reactors under test. No attempt is made to compare and contrast the values of k and K reported here to the many different values reported by others.

Over the years, a number of different reaction mechanisms have been promoted to provide a rationale for the kinetics exhibited by most photocatalytic systems, as summarised by Eqs. (7) and (8), but no one model has gained general approval [2]. A typical example is the disrupted adsorption model proposed by Ollis [75] in which, k is indeed described by Eq. (7) and K is given by the following expression,

$$K = k_{ads}/(k_{des} + \beta\rho_{UV}^\theta) \quad (9)$$

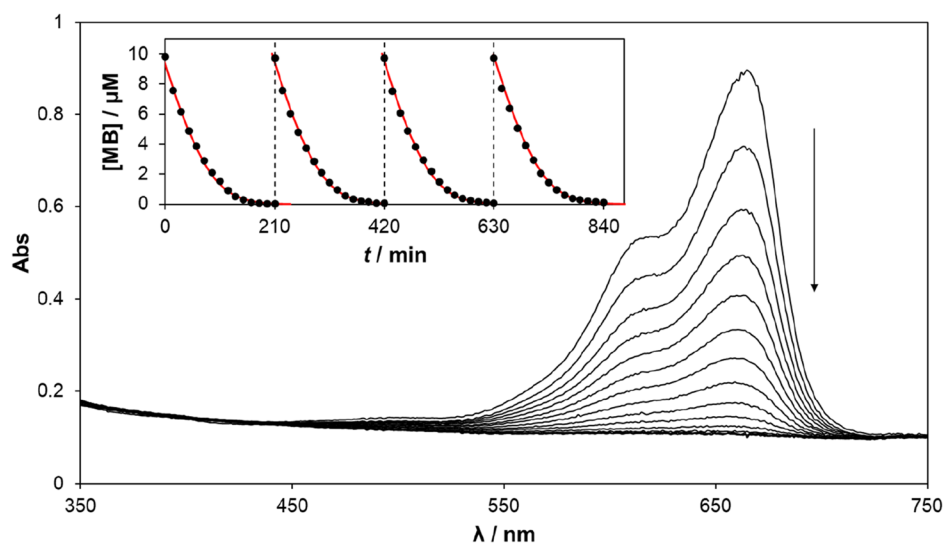
where, k_{ads} and k_{des} are the rate constants associated with the Langmuir adsorption and desorption of P onto the photocatalytic surface sites, so that their ratio, k_{ads}/k_{des} is equal to the Langmuir adsorption constant, K_L . In this, and in most other kinetic models, it is assumed that $[\text{O}_2]$ is constant and is incorporated in the proportionality constant that relates r to the other experimental parameters, ρ_{UV} and $[\text{P}]$ [2].

A study of the variation of the rate of reaction (1) as a function of ρ_{UV} , revealed a rate that gradually increases with ρ_{UV} , as illustrated by the plot of r vs ρ_{UV} , in Fig. S6 of the ESI. In this Figure, the line of best fit to the data was generated using Eqs. (7)–(9) of the Ollis disrupted adsorption model [75] and a value of $\theta = 0.58$. According to the Ollis model, at high irradiance values, where the recombination of photogenerated electron-hole pairs dominates, $\theta = 0.5$, whereas as low values of, $\theta = 1.0$, since electron-hole recombination is a minor process [2, 75]. Thus, the line of best fit value of 0.58 for θ to the data in Fig. S6 is consistent with the high irradiance value, i.e. 15mw cm^{-2} , used in this work.

3.3 Photocatalytic reactor A: circulating flow system studies

By making the waste tank and supply reservoir one and the same, the single pass test system, illustrated in Fig. 4, was converted into a more usually reported circulating flow photocatalytic reactor system, a schematic of which is illustrated

Fig. 6 Recorded absorption spectra of the 10 μM MB acidic aqueous solution (0.01 M HCl) flowing through photocatalytic reactor **A** (UV pre-conditioned for 168 h) in circulating flow mode, $f=40\text{ cm}^3\text{ min}^{-1}$; the spectra were recorded every 15 min. The total reaction solution volume was 10 cm^3 and the UVA irradiance, ρ , was 15 mW cm^{-2} . The insert plot is that of a sequence of four [MB] vs irradiation time, t , plots recorded using the same reactor, in which the first decay trace was been derived from the variation in ΔAbs_{665} as a function of t derived from the absorbance data in the main diagram



in Fig. S7 in the ESI. This system was used to demonstrate the ability of the photocatalytic reactor to photocatalyse reaction (1) repeatably with little or no loss in activity. Thus, in a series of repeat runs, the photocatalytic bleaching of 10 cm^3 of a 10 μM MB acidic aqueous solution (0.01 M HCl), was carried out using the same photocatalytic reactor **A** as employed above in single pass mode, but in circulating flow mode, with $f=40\text{ cm}^3\text{ min}^{-1}$. The absorption spectrum of the MB reaction solution was recorded at 15 min intervals during the UV irradiation of the reactor and the results for the first run are illustrated in Fig. 6 and show a continual loss in colour with UV irradiation time, t . Other work shows that in the absence of the TiO_2/PLA lining the MB concentration remains unchanged with illumination time. From the spectral data illustrated in Fig. 6, a plot was constructed of the variation in ΔAbs_{665} , and so [MB], as a function of irradiation time, t . This experiment was repeated three more times using the same reactor, and the results, in the form of a sequence of [MB] vs t decays are illustrated in the insert diagram in Fig. 6.

In this work, the integrated form of Eq. (7), i.e.

$$\ln\left(\frac{[\text{MB}]_0}{[\text{MB}]_t}\right) + K([\text{MB}]_0 - [\text{MB}]_t) = kKt \quad (10)$$

was used to analyse the [MB] vs t decay plots illustrated in Fig. 6, where $[\text{MB}]_0$ and $[\text{MB}]_t$ are the concentrations of MB at the start and after irradiation time t , respectively. Thus, in the insert plot in Fig. 6, the red line in each of the decay profiles is that of the best fit to Eq. (7) with k and K equal to $0.19\text{ }\mu\text{M min}^{-1}$ and $0.19\text{ }\mu\text{M}^{-1}$, respectively. Note that the near identical shapes of the repeat irradiation decay curves illustrated in Fig. 6, suggest that the 168 h UV pre-conditioning time, identified using the TiO_2/PLA rectangular films, when applied to the reactor also produces a TiO_2/PLA lining of optimum activity, since if this was not the case,

it would be expected that k would increase with increasing run number, especially given the UV irradiance in the kinetics runs, 15 mW cm^{-2} is 10 \times 's that used in the UV pre-conditioning process.

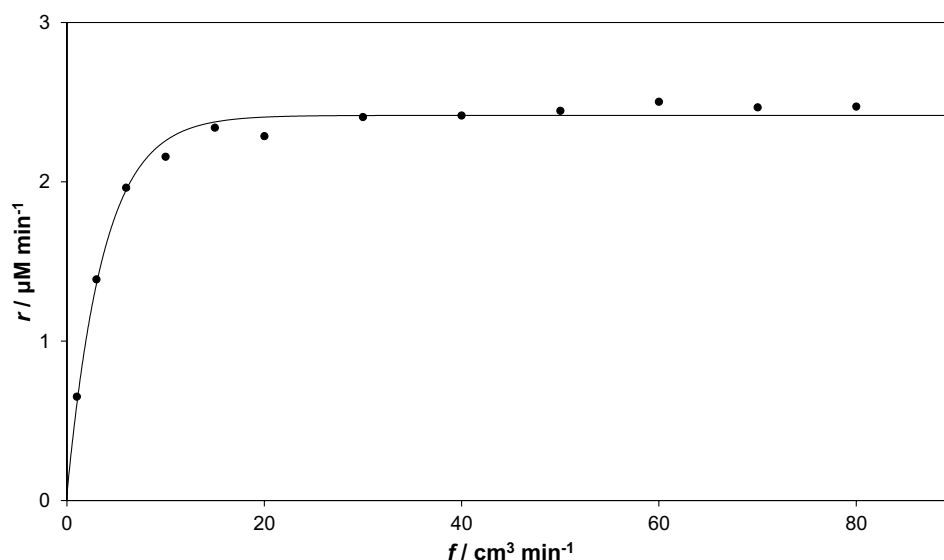
The dark Langmuir adsorption isotherm for MB, K_L , on P25 TiO_2 has been studied by Matthews who reports a value of ca. $0.0295\text{ }\mu\text{M}^{-1}$, i.e. ca 6.5 \times 's smaller than that found here for K [64]. However, as noted earlier, K is just a constant used to fit the data and, in all the proposed mechanisms for photocatalysis [2], is not simply related to K_L ; as indicated by Eq. (9) for the Ollis disrupted adsorption model [75]. Although, it is worth noting that in most photocatalytic studies, K is found to be $\gg K_L$, as it is here, and this feature needs to be addressed in any proposed reaction photocatalysis mechanism [2].

3.4 Photocatalytic reactor B: single pass and circulating flow studies

As noted earlier, the other 3D printed photocatalytic reactor, Reactor **B**, differed only from that of reactor **A**, in that it had an additional 35 equally spaced, quarter circle-shaped PLA baffles, as illustrated in Fig. S1 in the ESI. This reactor was printed and tested to show how easy it is to modify the design of a 3D printed photocatalytic reactor. In this work, although the added feature, i.e. baffles, is very simple, it is very unusual to find them in most reported examples of fixed-film photocatalytic reactors, probably because they are difficult to add to reactors constructed of glass or metal.

The baffles were added to reactor **A**, to create reactor **B**, to promote lateral mixing of the laminar flow streams and so produce a reactor with a lower dependence upon mass transport kinetics [76]. The efficacy of the baffles in reactor **B** in this respect was readily demonstrated by studying the rate of reaction (1), r , as a function of f , in single pass mode,

Fig. 7 Measured average rate of MB photocatalysed bleaching, r , as a function of reaction solution flow rate, f , determined using reactor **B** (UV pre-conditioned for 168 h) in single pass mode, with all other conditions as those used to generate the parallel set of data for reactor **A** illustrated in Fig. 5



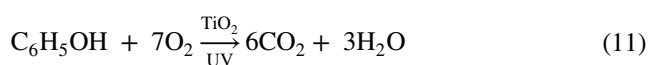
under otherwise identical conditions as used to generate the data in Fig. 5 for the *without-baffles* reactor **A**. The results of this work are illustrated in Fig. 7, and reveal that for reactor **B** the measured rate appears largely independent of flow rate at values as low as $15 \text{ cm}^3 \text{ min}^{-1}$, i.e. much lower than that found for reactor **A**, with its threshold value of $f = 40 \text{ cm}^3 \text{ min}^{-1}$.

Reactor **B** was then used in circulating flow mode, under the same conditions to generate the same data set type as illustrated in Fig. 6 for reactor **A**, but with $f = 15$, rather than $40 \text{ cm}^3 \text{ min}^{-1}$. As might be expected, if there is no mass transport component to the measured reaction rate, r , the results of this work for reactor **B**, were found to be near identical to those for reactor **A**, see Fig. 6, and are illustrated in Fig. S8 in the ESI. Each decay profile gave a good fit to Eq. (7), with k and K values of $0.15 \mu\text{M min}^{-1}$ and $0.19 \mu\text{M}^{-1}$, respectively. It is interesting, although perhaps not surprising, that the calculated values of K for both reactors **A** and **B** were found to be the same, given that the TiO_2/PLA coatings were identical. The slightly lower value of k (0.15 , cf 0.19 , $\mu\text{M min}^{-1}$) for reactor **B**, compared to **A**, is probably due to the reduction of the surface area of, and the incident UV irradiance that impinges on, reactor **B**'s TiO_2/PLA lining, caused by the presence of the 35 baffles.

3.5 Photocatalytic destruction of phenol

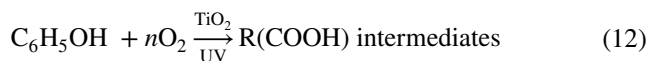
Although methylene blue remains a popular choice as a test pollutant [26–41], it is hardly a common organic pollutant of wastewater. In contrast, phenols are common pollutants of wastewater and are derived from a myriad of sources including, paint, pesticides and the petrochemical industries [77]. It is perhaps no surprise, therefore, that phenol, PhOH , is regularly used as a test organic pollutant in photocatalysis

[42–51] and, along with 4-chlorophenol, is the basis of most of the detailed kinetic studies of the photocatalytic process [2]. The overall oxidative mineralisation of phenol photocatalysed by TiO_2 can be summarised as follows,



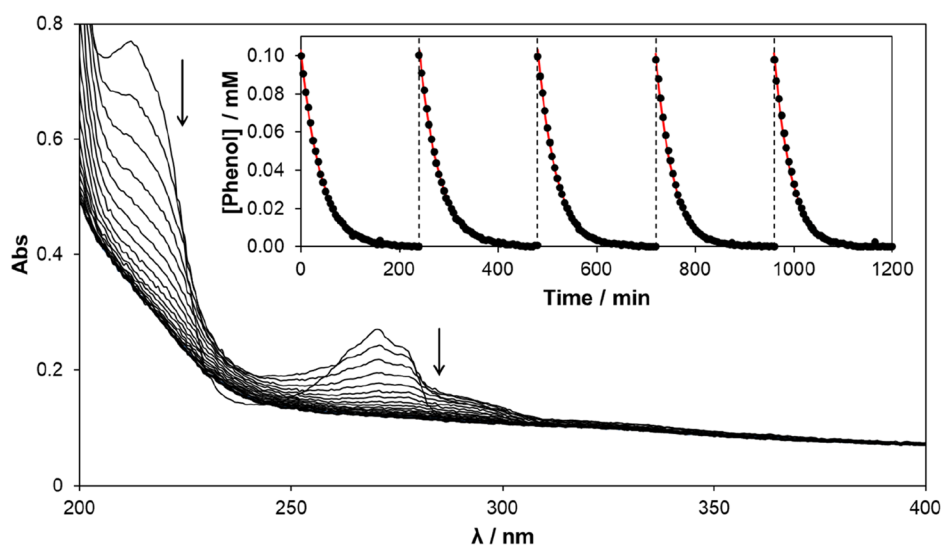
Mechanistic studies of reaction (11) reveal that the main aromatic intermediates generated are catechol, hydroquinone and benzophenone [78], but that these are always present at much lower concentrations than PhOH , as they are rapidly further oxidised to aliphatic carboxylic acids, i.e. $\text{R}(\text{COOH})$, such as muconic and 3 hydroxypropyl acid, which in turn are eventually oxidised to CO_2 and H_2O [77].

Usually, the photocatalytic oxidation of phenol is monitored using HPLC, which allows both the disappearance of phenol, and the subsequent appearance of the low initial hydroxylated intermediates to be followed. However, as demonstrated by others [6], it is also possible to monitor the destruction of the phenol, albeit more crudely, *via* the disappearance of the UV/Vis absorption band due to its $\pi \rightarrow \pi^*$ transition at ca. 270 nm [79]. Under such conditions, it follows that the photocatalytic reaction is more appropriately described by the following reaction equation,



A brief inspection of photocatalytic reactions (1) and (12) reveals they are very similar in that they are both bleaching processes, due to a loss of conjugation *via* an initial oxidative process, which can be monitored spectrophotometrically. Thus, under otherwise identical conditions to those used to generate the results in Fig. 6 for MB, photocatalytic reactor **A** in circulating flow mode was used to mediate reaction (12)

Fig. 8 Measured absorption spectra of a 100 μM PhOH aqueous flowing through photocatalytic reactor **A** in circulating flow mode, $f=40\text{ cm}^3\text{ min}^{-1}$; the spectra were recorded as a function of irradiation time every 15 min. The total reaction solution volume was 9 cm^3 and $\rho = 40\text{ mW cm}^{-2}$. The insert plot is that of $[\text{PhOH}]$ vs irradiation time, t , recorded for the same reactor five times, in which the first decay trace has been derived from the variation in ΔAbs_{270} as a function of t using spectral data from the main diagram



and the resulting measured change in the UV/Vis absorption spectrum of the circulating reaction solution as a function of different UV irradiation times is illustrated in Fig. 8. In this work, a UV irradiance of 40 mW cm^{-2} was employed to drive the reaction over a time span similar to that found when using MB, i.e. $< 220\text{ min}$. The spectroscopic data in Fig. 8 shows that the characteristic peaks due to PhOH in aqueous solution at 213 and 270 nm decrease with increasing UV irradiation time in accordance with reaction (12). The molar absorptivity of PhOH at 270 nm was determined as $1500\text{ M}^{-1}\text{ cm}^{-1}$ and was used to convert the measured absorbance at this wavelength of the reaction solution at each irradiance time, t , to the associated value of $[\text{PhOH}]$.

The same reactor was used 5 times in series to photocatalyse reaction (12), each time using an initial $[\text{PhOH}] = 100\text{ }\mu\text{M}$, and the results of this work are illustrated in the insert diagram in Fig. 8. In each case, the decay in $[\text{PhOH}]$ as a function of t was found to fit first order kinetics, with a first order rate constant, $k_1 = 0.029\text{ min}^{-1}$. The identical form of the 5 decay curves shows that, albeit under these limited test conditions, the photocatalytic reactor does not lose activity with repeated use.

First order decay kinetics is not uncommon in semiconductor photocatalysis and can be readily derived from the saturation kinetics equation, Eq. (7), assuming $K[\text{pollutant}] \ll 1$. The observation of first order kinetics for reaction (12) is consistent with previous studies on circulating flow photocatalytic reactors which have used PhOH as the test pollutant [6, 80]. In this work, given $k_1 = 0.029\text{ min}^{-1}$ and $[\text{PhOH}]_0 = 100\text{ }\mu\text{M}$, it follows that $r = 2.9\text{ }\mu\text{M min}^{-1}$, which then allows a value of 0.052% to be calculated for δ using Eq. (6), given $\rho = 40 \times 0.6 = 24\text{ mW cm}^{-2}$, $Vr = 8.8\text{ cm}^3$, $A_r = 11.2\text{ cm}^2$. This value is approximately twice that calculated for reaction (1), i.e. 0.025%, using the same reactor, probably because

the initial concentration of test organic pollutant, PhOH, was $10\times$'s greater, i.e. $100\text{ cf } 10\text{ }\mu\text{M}$.

In another piece of work, the measured value of k_1 for reaction (12) was found to be unchanged when reactor **A**, in circulating flow mode, was run at either 40 or $15\text{ cm}^3\text{ min}^{-1}$, indicating that the reaction kinetics at both these flow rates is largely activation-controlled, i.e. had no major mass transport component. If this were not the case then r would have been expected to decrease with decreasing f . In contrast, under the same conditions, using the same reactor, the photocatalysed bleaching of MB was found to be slower at $15\text{ cm}^3\text{ min}^{-1}$, than at $40\text{ cm}^3\text{ min}^{-1}$, as expected given the dependence of r vs f for this reactor illustrated in Fig. 5. The reason why the photocatalysed bleaching of phenol, i.e. reaction (12), does not exhibit the same flow rate sensitivity in reactor **A** as show by MB and reaction (1), is because the initial $[\text{PhOH}]$ employed was $10\times$'s that of $[\text{MB}]$ and it is known that the higher the reactant concentration the less likely mass transport controlled kinetics [81].

3.6 Photocatalytic space-time yield (PSTY)

Leblebici et al. [5] have suggested that the photocatalytic space-time yield, PSTY, of a reactor helps in the assessment of the performances of different reactors. The key parameters in the calculation a reactor's PSTY is (i) the standardised space time yield, STY, which is equal to the estimated volume (in m^3) of wastewater that would be processed when the pollutant concentration changes from 100 to 0.1 mM after 1 day of illumination and (ii) the lamp power, PL, scaled to the value that would illuminate 1 m^3 of the reactor. In our work, in which reactors **A** and **B** were operated in a loop,

Table 1 Relevant data and calculated STY, PL and PSTY values for reactor A

Parameter/pollutant	MB	PhOH
Rate/($\mu\text{M min}^{-1}$)	0.19	2.9
[Pollutant] ₀ / μM	10	100
k/day^{-1}	27.4	41.8
STY/(m^3 of reaction solution m^{-3} reactor volume day^{-1})	0.027	0.042
Lamp power/W	2.8	2.8
Total reaction solution volume/ cm^3	10	10
V_T/m^3	0.00001	0.00001
PL/(kW m^{-3} reactor volume)	280	280
PSTY/(m^3 of reaction solution m^{-3} reactor volume $\text{day}^{-1} \text{kW}^{-1}$)	0.98×10^{-4}	1.49×10^{-4}

Table 2 Reported PSTY values for immobilised photocatalyst reactors [5]

Reactor type	Pollutant	PSTY
Micro	Cortisone acetate	1.08×10^{-2}
Parallel plate	PhOH	1.03×10^{-3}
3D printed PFR ^a	PhOH	1.49×10^{-4}
3D printed PFR ^a	MB	0.98×10^{-4}
Foam	Diuron	4.61×10^{-5}
Capillary array	Methyl orange	1.15×10^{-6}

^aThis work

$$\text{STY} = k/999 \quad (13)$$

where k (units: day^{-1}) is the apparent first order rate constant, and

$$\text{PL} = P/V_T \quad (14)$$

where P is the lamp power used in the experimental work (in kW) and V_T is the total volume of the reaction solution (in m^3). The value of PSTY is then taken as,

$$\text{PSTY} = \text{STY}/\text{PL} \quad (15)$$

The values of the various parameters and the calculated values for STY, PL and PSTY, using MB and PhOH for reactor A are given in Table 1.

As the value of the rate for MB removal *via* reaction (1) using reactor B was similar to that for reactor A, i.e. 0.15 of $0.19 \mu\text{M min}^{-1}$, the associated value of PSTY was not calculated. It is useful to briefly consider who the calculated value of PSTY for reactor A, compares with those calculated for other reactors, a short list of which is given in Table 2. The best performing of the immobilised reactors is a microreactor, which is not too surprising given its high area-to-volume feature, even though its illumination was far from optimised;

with optimisation Lelebeci et al. suggest a PSTY value of 13 might be possible [5]. The performance of this first reported 3D printed photoreactor is encouraging, given its mid-range PSTY value compared to other reactor types, see Table 2. 3D printing could, of course be used to print a microreactor, which is likely to generate a much higher PSTY higher value, but with scale up would present a significant challenge with regard efficient light distribution [5].

4 Conclusions

Two types of lab-scale, sinusoidal, 3D printed plastic photocatalytic reactors are described, which are identical in all aspects except that one has no baffles, reactor A, whereas the other has baffles, reactor B. Both reactors are lined with a P25 TiO_2 /polylactic acid (PLA) coating, which, after UVA pre-conditioning, is able to photocatalyse the bleaching of circulating aqueous solutions of MB and PhOH, repeatedly, without any obvious loss of activity. The rate of the photocatalysed bleaching of MB exhibited by reactor B shows a much lower dependence upon flow rate than reactor A, due to the greater lateral mixing of the laminar flow streams produced by the baffles.

This work demonstrates that 3D printing can be used to generate quickly, cheaply and reproducibly different designs of a photocatalytic reactor that are able to effect the photocatalytic destruction of test pollutants in an aqueous solution. 3D printing is a scalable process and so such reactors, when produced on an appropriate scale, may find commercial application. However, it is not clear how much a hindrance the UV-pre-activation step will be in the future to the scaled-up utilisation of 3D printed photocatalytic reactors. It is possible, for example, that this pre-conditioning could be carried out before the photocatalytic lining is sealed onto the PLA window and that it could be accelerated markedly using higher irradiance, lower wavelength UV radiation, in the presence of a much stronger oxidant than O_2 , such as O_3 . In addition, if the reactor lifetime proves significant (many months or years) then a relatively short period, such as 7 days, for it to become fully activated, may prove acceptable. Certainly, many current photocatalytic products, such as paints and fabrics, require days, if not weeks, of exposure to the ambient UV, usually solar, before they start to exhibit significant activity [56–59].

Although it now appears very unlikely that photocatalysis can be used for the large-scale treatment of wastewater, there appear plenty of opportunities for its use in niche applications [82], especially for an inexpensive, easy to produce and use photocatalytic reactor, such as can be generated by 3D printing. One area of potential application appears to be treatment of wastewater streams from aquaculture and hydroponics, as both are often carried out on a relatively

small scale. Another potential area of application is the solar disinfection of drinking water, i.e. SODIS [83, 84]. Work exploring these potential areas of application is progress, along with more rigorous studies into the performance of 3D reactors, including reactor design, scale up, modelling, prolonged durability, the use of other, more refractory pollutants and irradiation optimisation.

Supplementary Information The online version contains supplementary material available at <https://doi.org/10.1007/s43630-022-00242-y>.

Acknowledgement AM thanks the US-Ireland R&D Partnership (USI 132) and COR thank the Catalysis Hub funded by EPSRC grant referenceEP/R026645/1, for supporting this work.

Declarations

Conflict of interest On behalf of all authors, the corresponding author states that there is no conflict of interest.

Open Access This article is licensed under a Creative Commons Attribution 4.0 International License, which permits use, sharing, adaptation, distribution and reproduction in any medium or format, as long as you give appropriate credit to the original author(s) and the source, provide a link to the Creative Commons licence, and indicate if changes were made. The images or other third party material in this article are included in the article's Creative Commons licence, unless indicated otherwise in a credit line to the material. If material is not included in the article's Creative Commons licence and your intended use is not permitted by statutory regulation or exceeds the permitted use, you will need to obtain permission directly from the copyright holder. To view a copy of this licence, visit <http://creativecommons.org/licenses/by/4.0/>.

References

- Wang, D., Mueses, M. A., Márquez, J. A. C., Machuca-Martínez, F., Grčić, I., Moreira, R. P. M., & Puma, G. L. (2021). Engineering and modeling perspectives on photocatalytic reactors for water treatment. *Water Research*, 202, 117421. <https://doi.org/10.1016/j.watres.2021.117421>
- Mills, A., O'Rourke, C., & Moore, K. (2015). Powder semiconductor photocatalysis in aqueous solution: An overview of kinetics-based reaction mechanisms. *Journal of Photochemistry and Photobiology A: Chemistry*, 310, 66–105. <https://doi.org/10.1016/j.jphotochem.2015.04.011>
- Braham, R. J., & Harris, A. T. (2009). Review of major design and scale-up considerations for solar photocatalytic reactors. *Industrial & Engineering Chemistry Research*, 48, 8890–8905. <https://doi.org/10.1021/ie900859z>
- Balasubramanian, G., Dionysiou, D. D., Suidan, M. T., Baudin, I., & Lafné, J.-M. (2004). Evaluating the activities of immobilized TiO₂ powder films for the photocatalytic degradation of organic contaminants in water. *Applied Catalysis B: Environmental*, 47, 73–84. <https://doi.org/10.1016/j.apcatb.2003.04.002>
- Leblebici, M. E., Stefanidis, G. D., & Gerven, T. V. (2015). Comparison of photocatalytic space-time yields of 12 reactor designs for wastewater treatment. *Chemical Engineering and Processing: Process Intensification*, 97, 106–111. <https://doi.org/10.1016/j.cep.2015.09.009>
- Matthews, R. W. (1987). Photooxidation of organic impurities in water using thin films of titanium dioxide. *Journal of Physical Chemistry*, 91, 3328–3333. <https://doi.org/10.1021/j100296a044>
- Qiu, W., & Zheng, Y. (2007). A comprehensive assessment of supported titania photocatalysts in a fluidized bed photoreactor: Photocatalytic activity and adherence stability. *Applied Catalysis B: Environmental*, 71, 151–162. <https://doi.org/10.1016/j.apcatb.2006.08.021>
- Chen, Y., & Dionysiou, D. D. (2006). TiO₂ photocatalytic films on stainless steel: The role of Degussa P-25 in modified sol–gel methods. *Applied Catalysis B: Environmental*, 62, 255–264. <https://doi.org/10.1016/j.apcatb.2005.07.017>
- Byrne, J. A., Eggins, B. R., Brown, N. M. D., McKinney, B., & Rouse, M. (1998). Immobilisation of TiO₂ powder for the treatment of polluted water. *Applied Catalysis B: Environmental*, 17, 25–36. [https://doi.org/10.1016/S0926-3373\(97\)00101-X](https://doi.org/10.1016/S0926-3373(97)00101-X)
- Fernandez-Ibañez, P., Malato, S., & Enea, O. (1999). Photoelectrochemical reactors for the solar decontamination of water. *Catalysis Today*, 54, 329–339. [https://doi.org/10.1016/S0920-5861\(99\)00194-7](https://doi.org/10.1016/S0920-5861(99)00194-7)
- Kavan, L., O'Regan, B., Kay, A., & Grätzel, M. (1993). Preparation of TiO₂ (anatase) films on electrodes by anodic oxidative hydrolysis of TiCl₃. *Journal of Electroanalytical Chemistry*, 346, 291–307. [https://doi.org/10.1016/0022-0728\(93\)85020-H](https://doi.org/10.1016/0022-0728(93)85020-H)
- Fateh, R., Dillert, R., & Bahnemann, D. (2014). Self-cleaning properties, mechanical stability, and adhesion strength of transparent photocatalytic TiO₂–ZnO coatings on polycarbonate. *ACS Applied Materials & Interfaces*, 6, 2270–2278. <https://doi.org/10.1021/am4051876>
- Kanazawa, T., & Ohmori, A. (2005). Behavior of TiO₂ coating formation on PET plate by plasma spraying and evaluation of coating's photocatalytic activity. *Surface and Coatings Technology*, 197, 45–50. <https://doi.org/10.1016/j.surfcoat.2004.09.029>
- Chawengkijwanicha, C., & Hayata, Y. (2008). Development of TiO₂ powder-coated food packaging film and its ability to inactivate Escherichia coli in vitro and in actual tests. *International Journal of Food Microbiology*, 123, 288–292. <https://doi.org/10.1016/j.ijfoodmicro.2007.12.017>
- Ratova, M., West, G. T., & Kelly, P. J. (2014). Optimisation of HiPIMS photocatalytic titania coatings for low temperature deposition. *Surface and Coatings Technology*, 250, 7–13. <https://doi.org/10.1016/j.surfcoat.2014.02.020>
- Lee, C.-S., Kim, J., Son, J. Y., Choi, W., & Kim, H. (2009). Photocatalytic functional coatings of TiO₂ thin films on polymer substrate by plasma enhanced atomic layer deposition. *Applied Catalysis B: Environmental*, 91, 628–633. <https://doi.org/10.1016/j.apcatb.2009.06.037>
- Bodaghia, H., Mostofi, Y., Oromiehie, A., Zamani, Z., Ghanbarzadeh, B., Costa, C., Conte, A., & Nobile, M. A. D. (2013). Evaluation of the photocatalytic antimicrobial effects of a TiO₂ nanocomposite food packaging film by in vitro and in vivo tests. *LWT - Food Science and Technology*, 50, 702–706. <https://doi.org/10.1016/j.lwt.2012.07.027>
- Ratova, M., & Mills, A. (2015). Antibacterial titania-based photocatalytic extruded plastic films. *Journal of Photochemistry and Photobiology A: Chemistry*, 299, 159–165. <https://doi.org/10.1016/j.jphotochem.2014.11.014>
- Martín de Vidales, M. J., Nieto-Márquez, A., Morcuende, D., Atanes, E., Blaya, F., Soriano, E., & Fernández-Martínez, F. (2019). 3D printed floating photocatalysts for wastewater treatment. *Catalysis Today*, 328, 157–163. <https://doi.org/10.1016/j.cattod.2019.01.074>
- Wikipedia, *Applications of 3D printing*. Retrieved April 2022, from https://en.wikipedia.org/wiki/Applications_of_3D_printing.
- Skorski, M. R., Esenther, J. M., Ahmed, Z., Miller, A. E., & Hartings, M. R. (2016). The chemical, mechanical, and physical

- properties of 3D printed materials composed of TiO₂-ABS nanocomposites. *Science and Technology of Advanced Materials*, 17, 89–97. <https://doi.org/10.1080/14686996.2016.1152879>
22. Jo, W., Yoon, B. J., Lee, H., & Moon, M. W. (2017). 3D printed hierarchical gyroid structure with embedded photocatalyst TiO₂ nanoparticles. *3D Printing and Additive Manufacturing*, 4, 222–230. <https://doi.org/10.1089/3dp.2017.0033>
 23. Sangiorgi, A., Gonzalez, Z., Ferrandez-Montero, A., Yus, J., Sanchez-Herencia, A. J., Galassi, C., Sanson, A., & Ferrari, B. (2019). 3D printing of photocatalytic filters using a biopolymer to immobilize TiO₂ nanoparticles. *Journal of the Electrochemical Society*, 166, H3239–H3248. <https://doi.org/10.1149/2.0341905jes>
 24. Son, S., Jung, P.-H., Park, J., Chae, D., Huh, D., Byun, M., Ju, S., & Lee, H. (2018). Customizable 3D-printed architecture with ZnO-based hierarchical structures for enhanced photocatalytic performance. *Nanoscale*, 10, 21696–21702. <https://doi.org/10.1039/C8NR06788K>
 25. Viskadourakis, Z., Sevastaki, M., & Kenanakis, G. (2018). 3D structured nanocomposites by FDM process: a novel approach for large-scale photocatalytic applications. *Applied Physics A: Materials Science and Processing*, 124, 1–8. <https://doi.org/10.1007/s00339-018-2014-6>
 26. Lindstrom, H., Wootton, R., & Iles, A. (2007). High surface area titania photocatalytic microfluidic reactors. *AIChE Journal*, 53, 695–702. <https://doi.org/10.1002/aic.11096>
 27. López, A., Acosta, D., Martínez, A. I., & Santiago, J. (2010). Nanostructured low crystallized titanium dioxide thin films with good photocatalytic activity. *Powder Technology*, 202, 111–117. <https://doi.org/10.1016/j.powtec.2010.04.025>
 28. Horng, R. Y., Chang, M. C., Shao, H., Hu, Y. J., & Huang, C. P. (2007). The usage of non-woven fabric material as separation media in submerged membrane photocatalytic reactor for degradation of organic pollutants in water. *Separation Science and Technology*, 42, 1381–1390. <https://doi.org/10.1080/01496390701289765>
 29. Ryu, J., Choi, W., & Choo, K. H. (2005). A pilot-scale photocatalyst-membrane hybrid reactor: Performance and characterization. *Water Science and Technology*, 51, 491–497. <https://doi.org/10.2166/wst.2005.0672>
 30. Xue, X., Zang, W., Deng, P., Wang, Q., Xing, L., Zhang, Y., & Wang, Z. L. (2015). Piezo-potential enhanced photocatalytic degradation of organic dye using ZnO nanowires. *Nano Energy*, 13, 414–422. <https://doi.org/10.1016/j.nanoen.2015.02.029>
 31. Ochoa-Gutiérrez, K. S., Tabares-Aguilar, E., Mueses, M. Á., Machuca-Martínez, F., & Li-Puma, G. (2018). A Novel Prototype Offset Multi Tubular Photoreactor (OMTP) for solar photocatalytic degradation of water contaminants. *Chemical Engineering Journal*, 341, 628–638. <https://doi.org/10.1016/j.cej.2018.02.068>
 32. Vaiano, V., Sacco, O., Pisano, D., Sannino, D., & Ciambelli, P. (2015). From the design to the development of a continuous fixed bed photoreactor for photocatalytic degradation of organic pollutants in wastewater. *Chemical Engineering Science*, 137, 152–160. <https://doi.org/10.1016/j.ces.2015.06.023>
 33. Di Capua, G., Femia, N., Migliaro, M., Sacco, O., Sannino, D., Stoyka, K., & Vaiano, V. (2017). Intensification of a flat-plate photocatalytic reactor performances by innovative visible light modulation techniques: A proof of concept. *Chemical Engineering and Processing: Process Intensification*, 118, 117–123. <https://doi.org/10.1016/j.cep.2017.05.004>
 34. Sutisna, Rokhmat, M., Wibowo, E., Khairurrijal, & Abdullah, M. (2017). Prototype of a flat-panel photoreactor using TiO₂ nanoparticles coated on transparent granules for the degradation of Methylene Blue under solar illumination. *Sustainable Environment Research*, 27, 172–180. <https://doi.org/10.1016/j.serj.2017.04.002>
 35. Sutisna, Rokhmat, M., Wibowo, E., Murniati, R., Khairurrijal, & Abdullah, M. (2017). Novel solar photocatalytic reactor for wastewater treatment. *IOP Conference Series: Materials Science and Engineering*, 214, 012010. <https://doi.org/10.1088/1757-899X/214/1/012010>
 36. Zhang, C., Sabouni, R., Shao, Y., & Gomaa, H. G. (2017). Performance of submerged oscillatory membrane photoreactor for water treatment. *Journal of Environmental Chemical Engineering*, 5, 3330–3336. <https://doi.org/10.1016/j.jece.2017.06.046>
 37. El-Mekkawi, D. M., Nady, N., Abdelwahab, N. A., Mohamed, W. A. A., & Abdel-Mottaleb, M. S. A. (2016). Flexible bench-scale recirculating flow CPC photoreactor for solar photocatalytic degradation of methylene blue using removable TiO₂ immobilized on PET sheets. *International Journal of Photoenergy*, 2016, 9270492. <https://doi.org/10.1155/2016/9270492>
 38. El-Mekkawi, D. M., Abdelwahab, N. A., Mohamed, W. A. A., Taha, N. A., & Abdel-Mottaleb, M. S. A. (2020). Solar photocatalytic treatment of industrial wastewater utilizing recycled polymeric disposals as TiO₂ supports. *Journal of Cleaner Production*, 249, 119430. <https://doi.org/10.1016/j.jclepro.2019.119430>
 39. Teekateerawej, S., Nishino, J., & Nosaka, Y. (2006). Design and evaluation of photocatalytic micro-channel reactors using TiO₂-coated porous ceramics. *Journal of Photochemistry and Photobiology A: Chemistry*, 179, 263–268. <https://doi.org/10.1016/j.jphotochem.2005.08.024>
 40. Claes, T., Dilissen, A., Leblebici, M. E., & Van Gerven, T. (2019). Translucent packed bed structures for high throughput photocatalytic reactors. *Chemical Engineering Journal*, 361, 725–735. <https://doi.org/10.1016/j.cej.2018.12.107>
 41. Sacco, O., Sannino, D., & Vaiano, V. (2019). Packed bed photoreactor for the removal of water pollutants using visible light emitting diodes. *Applied Sciences*, 9, 472. <https://doi.org/10.3390/app9030472>
 42. Sobczykński, A., Gimenez, J., & Cervera-March, S. (1997). Photodecomposition of phenol in a flow reactor: adsorption and kinetics. *Monatshefte für Chemie - Chemical Monthly*, 128, 1109–1118. <https://doi.org/10.1007/BF00807561>
 43. Souzanchi, S., Vahabzadeh, F., Fazel, S., & Hosseini, S. N. (2013). Performance of an annular sieve-plate column photoreactor using immobilized TiO₂ on stainless steel support for phenol degradation. *Chemical Engineering Journal*, 223, 268–276. <https://doi.org/10.1016/j.cej.2013.02.123>
 44. Mirzaei, M., Jafarikojour, M., Dabir, B., & Dadvar, M. (2017). Evaluation and modeling of a spinning disc photoreactor for degradation of phenol: Impact of geometry modification. *Journal of Photochemistry and Photobiology A: Chemistry*, 346, 206–214. <https://doi.org/10.1016/j.jphotochem.2017.05.043>
 45. Meunier, S. M., Zhang, Z., Gamage, J., & Duvnjak, Z. (2010). Design and characterization of a novel rotating corrugated drum reactor for wastewater treatment. *International Journal of Photoenergy*, 2010, 146743. <https://doi.org/10.1155/2010/146743>
 46. Vezzoli, M., Martens, W. N., & Bell, J. M. (2011). Investigation of phenol degradation: True reaction kinetics on fixed film titanium dioxide photocatalyst. *Applied Catalysis A, General*, 404, 155–163. <https://doi.org/10.1016/j.apcata.2011.07.025>
 47. Leblebici, M. E., Rongé, J., Martens, J. A., Stefanidis, G. D., & Van Gerven, T. (2015). Computational modelling of a photocatalytic UV-LED reactor with internal mass and photon transfer consideration. *Chemical Engineering Journal*, 264, 962–970. <https://doi.org/10.1016/j.cej.2014.12.013>
 48. Krýsa, J., Waldner, G., Měšťánková, H., Jirkovský, J., & Grabner, G. (2006). Photocatalytic degradation of model organic pollutants on an immobilized particulate TiO₂ layer. Roles of adsorption processes and mechanistic complexity. *Applied Catalysis B*:

- Environmental*, 64, 290–301. <https://doi.org/10.1016/j.apcatb.2005.11.007>
49. Horng, R.-Y., Huang, C., Chang, M.-C., Shao, H., Shiau, B.-L., & Hu, Y.-J. (2009). Application of TiO₂ photocatalytic oxidation and non-woven membrane filtration hybrid system for degradation of 4-chlorophenol. *Desalination*, 245, 169–182.
 50. Haarstrick, A., Kut, O. M., & Heinzle, E. (1996). TiO₂-assisted degradation of environmentally relevant organic compounds in wastewater using a novel fluidized bed photoreactor. *Environmental Science & Technology*, 30, 817–824. <https://doi.org/10.1021/es9502278>
 51. Yatmaz, H. C., Wallis, C., & Howarth, C. R. (2001). The spinning disc reactor - Studies on a novel TiO₂ photocatalytic reactor. *Chemosphere*, 42, 397–403. [https://doi.org/10.1016/S0045-6535\(00\)00088-6](https://doi.org/10.1016/S0045-6535(00)00088-6)
 52. Liu, W., Zhou, J., Ma, Y., Wang, J., & Xu, J. (2017). Fabrication of PLA filaments and its printable performance. *IOP Conference Series: Materials Science and Engineering*, 275, 012033. <https://doi.org/10.1088/1757-899X/275/1/012033>
 53. Ranjan, N., Singh, R., & Ahuja, I. (2020). Development of PLA-Hap-CS-based biocompatible functional prototype: A case study. *Journal of Thermoplastic Composite Materials*, 33, 305–323.
 54. 3devo, 3devo support. Retrieved April 2022, from <https://support.3devo.com/recycled-pp-material-report/>.
 55. Mills Research Group, *3D Printed Reactor Gcode*. Retrieved April 2022, from <https://www.profandrewmills.com/2022/04/3d-printed-reactor-gcode/>.
 56. Baudys, M., Andrews, R., Han, R., O'Rourke, C., Hodgen, S., Krysa, J., & Mills, A. (2021). Photocatalytic paints for NO_x removal: Influence of various weathering conditions. *Journal of Environmental Chemical Engineering*, 9, 106172. <https://doi.org/10.1016/j.jece.2021.106172>
 57. STO. Retrieved April 2022, from <http://www.sto.co.uk/en/home/home.html>.
 58. Han, R., Andrews, R., O'Rourke, C., Hodgen, S., & Mills, A. (2021). Photocatalytic air purification: Effect of HNO₃ accumulation on NO_x and VOC removal. *Catalysis Today*, 380, 105–113. <https://doi.org/10.1016/j.cattod.2021.04.017>
 59. IKEA, *Meet GUNRID – the air purifying curtain*. Retrieved April 2022, from <https://ikea.today/meet-gunrid-air-purifying-curtain/>.
 60. ISO 10678:2010 (2010). Fine ceramics (advanced ceramics, advanced technical ceramics) Determination of photocatalytic activity of surfaces in an aqueous medium by degradation of methylene blue, ISO, Geneva. <https://www.iso.org/standard/46019.htm>.
 61. Mills, A., Hill, C., & Robertson, P. K. J. (2012). Overview of the current ISO tests for photocatalytic materials. *Journal of Photochemistry and Photobiology A: Chemistry*, 237, 7–23. <https://doi.org/10.1016/j.jphotochem.2012.02.024>
 62. Mills, A. (2012). An overview of the methylene blue ISO test for assessing the activities of photocatalytic films. *Applied Catalysis B: Environmental*, 128, 144–149. <https://doi.org/10.1016/j.apcatb.2012.01.019>
 63. Tschirch, J., Dillert, R., Bahnemann, D., Proft, B., Biedermann, A., & Goer, B. (2008). Photodegradation of methylene blue in water, a standard method to determine the activity of photocatalytic coatings? *Research on Chemical Intermediates*, 34, 381–392. <https://doi.org/10.1163/156856708784040588>
 64. Matthews, R. W. (1989). Photocatalytic oxidation and adsorption of methylene blue on thin films of near-ultraviolet-illuminated TiO₂. *Journal of the Chemical Society, Faraday Transactions, 1*(85), 1291–1302. <https://doi.org/10.1039/F19898501291>
 65. Houas, A., Lachheb, H., Ksibi, M., Elaloui, E., Guillard, C., & Herrmann, J.-M. (2001). Photocatalytic degradation pathway of methylene blue in water. *Applied Catalysis B: Environmental*, 31, 145–157. [https://doi.org/10.1016/S0926-3373\(00\)00276-9](https://doi.org/10.1016/S0926-3373(00)00276-9)
 66. Mills, A., Elliott, N., Hill, G., Fallis, D., Durrant, J. R., & Willis, R. L. (2003). Preparation and Characterisation of novel thick sol-gel titania film photocatalysts. *Photochemical and Photobiological Sciences*, 2, 591–596. <https://doi.org/10.1039/B212865A>
 67. Selifonov, A. A., Shapoval, O. G., Mikerov, A. N., & Tuchin, V. V. (2019). Determination of the diffusion coefficient of methylene blue solutions in dentin of a human tooth using reflectance spectroscopy and their antibacterial activity during laser exposure. *Optics and Spectroscopy*, 126, 758–768. <https://doi.org/10.1134/S0030400X19060213>
 68. The Electrochemical Society, *Electrochemistry Dictionary & Encyclopedia*. Retrieved April 2022, from <https://knowledge.electrochem.org/ed/dict.htm#d28>.
 69. Tham, C. Y., Hamid, Z. A. A., Ahmad, Z., & Hanafi, I. (2014). Surface modification of Poly(lactic acid) (PLA) via alkaline hydrolysis degradation. *Advanced Materials Research*, 970, 324–327. <https://doi.org/10.4028/www.scientific.net/AMR.970.324>
 70. Mills, A., & Crow, M. (2007). In situ, continuous monitoring of the photoinduced superhydrophilic effect: Influence of UV-type and ambient atmospheric and droplet composition. *The Journal of Physical Chemistry C*, 111, 6009–6016. <https://doi.org/10.1021/jp068327v>
 71. Turchi, C. S., & Ollis, D. F. (1988). Comment. Photocatalytic reactor design: an example of mass-transfer limitations with an immobilized catalyst. *Journal of Physical Chemistry*, 92, 6852–6853. <https://doi.org/10.1021/j100334a070>
 72. Hanekamp, H. B., & Nieuwkerk, H. J. V. (1980). Theoretical considerations on the performance of electrochemical flow-through detectors. *Analytica Chimica Acta*, 121, 13–22. [https://doi.org/10.1016/S0003-2670\(01\)84395-6](https://doi.org/10.1016/S0003-2670(01)84395-6)
 73. Wikipedia, *Reynolds number*. Retrieved April 2022 from https://en.wikipedia.org/wiki/Reynolds_number.
 74. Tschirch, J., Dillert, R., & Bahnemann, D. (2008). Photocatalytic degradation of methylene blue on fixed powder layers: which limitations are to be considered? *Journal of Advanced Oxidation Technologies*, 11, 193–198. <https://doi.org/10.1515/jaots-2008-0202>
 75. Ollis, D. (2005). Kinetics of liquid phase photocatalyzed reactions: an illuminating approach. *The Journal of Physical Chemistry B*, 109, 2439–2444. <https://doi.org/10.1021/jp040236f>
 76. Ollis, D. F., & Turchi, C. (1990). Heterogeneous photocatalysis for water purification: Contaminant mineralization kinetics and elementary reactor analysis. *Environmental Progress*, 9, 229–234. <https://doi.org/10.1002/ep.670090417>
 77. Grabowska, E., Reszczyńska, J., & Zaleska, A. (2012). Mechanism of phenol photodegradation in the presence of pure and modified-TiO₂: A review. *Water Research*, 46, 5453–5471. <https://doi.org/10.1016/j.watres.2012.07.048>
 78. Sobczykński, A., Duczmal, Ł., & Zmudziński, W. (2004). Phenol destruction by photocatalysis on TiO₂: An attempt to solve the reaction mechanism. *Journal of Molecular Catalysis A: Chemical*, 213, 225–230. <https://doi.org/10.1016/j.molcata.2003.12.006>
 79. Tetteh, S., Zuggle, R., Adotey, J. P. K., & Quashie, A. (2018). Electronic spectra of ortho-substituted phenols: An experimental and DFT study. *Journal of Spectroscopy*, 2018, 4193657. <https://doi.org/10.1155/2018/4193657>
 80. Dougna, A. A., Gombert, B., Kodom, T., Djaneye-Boundjou, G., Boukari, S. O. B., Leitner, N. K. V., & Bawa, L. M. (2015). Photocatalytic removal of phenol using titanium dioxide deposited on different substrates: Effect of inorganic oxidants. *Journal of Photochemistry and Photobiology A: Chemistry*, 305, 67–77. <https://doi.org/10.1016/j.jphotochem.2015.02.012>
 81. Ray, A. K., & Beenackers, A. A. C. M. (1997). Novel swirl-flow reactor for kinetic studies of semiconductor photocatalysis. *Environmental and Energy Engineering*, 43, 2571–2578. <https://doi.org/10.1002/aic.690431018>

82. Loeb, S. K., Alvarez, P. J. J., Brame, J. A., Cates, E. L., Choi, W., Crittenden, J., Dionysiou, D. D., Li, Q., Li-Puma, G., Quan, X., Sedlak, D. L., Waite, T. D., Westerhoff, P., & Kim, J.-H. (2019). The technology horizon for photocatalytic water treatment: sunrise or sunset? *Environmental Science & Technology*, *53*, 2937–2947. <https://doi.org/10.1021/acs.est.8b05041>
83. Byrne, J. A., Fernandez-Ibanez, P. A., Dunlop, P. S. M., Alrousan, D. M. A., & Hamilton, J. W. J. (2011). Photocatalytic enhancement for solar disinfection of water: A review. *International Journal of Photoenergy*, *2011*, 1–12. <https://doi.org/10.1155/2011/798051>
84. Wikipedia, *Solar water disinfection*. Retrieved April 2022 from https://en.wikipedia.org/wiki/Solar_water_disinfection.